PROCEEDINGS, 51st Workshop on Geothermal Reservoir Engineering
Stanford University, Stanford, California, February 9-11, 2026
SGP-TR-230

Evaluating Hydrogen Resource in Ultramafic, Mafic and Metamorphic Rocks

Marwah M. Alsinan, Ilenia Battiato and Anthony R. Kovscek

367 Panama St, Stanford, CA 94305

mms22@stanford.edu

Keywords: hydrogen; serpentinization; geochemistry; ultramafic

ABSTRACT

Hydrogen production in ultramafic, mafic and metamorphic rocks is limited by geochemical properties of rock and brine. These geochemical properties such as geochemical phases and molar compositions determine the maximum potential production of hydrogen from ultramafic rocks (resources). In this work, we use public geochemical data of ultramafic rocks from PetDB and in-house experiments (Ross et al., 2025) to evaluate variations in hydrogen resources at typical depths in the subsurface. We demonstrate a workflow for estimating hydrogen production from non-felsic igneous and metamorphic rocks that includes major oxide acquisition, mineral formula and endmember recalculation in MinplotX, and geochemical batch simulations of serpentinization across a range of hydrostatic pressures and geothermal temperatures. Our analysis indicates that the most optimal hydrogen production is at 10 km depth and forsterite composition below 0.9.

1. INTRODUCTION

The interaction between crustal fluids and iron-rich igneous and metamorphic basement rocks generates highly mobile hydrothermal fluids enriched with minerals and dissolved gases. For example, hydrogen, among other gases such as CO_2, H_2S, CH_4, N_2, Ar, and NH_3 is commonly produced in the non-condensable gas effluent in geothermal wells (Buck, 2025) and vent sites along the mid-Atlantic ridge (Bazarkina et al., 2020; Alsinan et al., 2025). These gases are routinely measured during exploration and production phases of fumaroles and geothermal wells to evaluate reservoir equilibrium temperature and for tracer testing. Powell (2000) provides a review of common gas geothermometers. In such geological settings, hydrothermal fluids are primarily expelled through buoyancy-driven thermal convection. During migration, these fluids may undergo phase separation into vapor and liquid, allowing them to accumulate in subsurface traps as geological hydrogen or to remain dissolved within geothermal reservoirs.

In this paper, we focus on hydrogen production from metamorphic and igneous source rocks, that exist naturally in the earth's crust between 5 and 20 km. Hydrogen can be generated naturally or artificially (e.g. enhanced geothermal system) through hydrothermal alteration of these source rocks at temperatures between 200 and 350 °C. Our objective is to evaluate hydrogen production from these source rocks at in-situ conditions using published olivine major oxide chemical composition data.

2. DATA ACQUISITION

We downloaded major oxide compositional data from the PetDB Database (www.earthchem.org/petdb) on October 21st, 2025 using parameters: feature name = country (USA) and sample type = Metamorphic or Igneous (plutonic: mafic or ultramafic) or (volcanic: mafic or ultramafic) (Fig. 1). The database showed several co-existing mineral phases, such as olivine, clinopyroxene, orthopyroxene, feldspar, ilmenite, chromite, calcite, garnet, kaersutite, glass and spinel. The total number of samples was 1311 (Fig. 1). However, we filtered the data by mineral phase olivine because olivine usually has the highest concentration of ferrous iron. Also, we filtered data by the electron probe microanalysis (EPMA) method because it is the standard for quantitative analysis of major oxide compositions for mineral formula and end-members recalculations (Walters, 2022; Walters & Gies, 2025). Although Scanning Electron Microscopy / Energy-Dispersive X-ray Spectroscopy (SEM-EDS) and X-ray diffraction (XRD) were available for some samples, they were not included in our analysis to maintain same level of consistency for all measurements. After filtration, we discarded 1138 samples and ended up with 173 samples out of the original 1311 samples. Then we acquired mineral phase chemical composition through the EarthChem API (https://ecapi.earthchem.org) because bulk download mis-assigns chemical composition to mineral phases. In addition to PetDB, we used EPMA measurements that were conducted in Stanford SUETRI-A lab (Ross et al., 2025) on Twin Sisters olivine sand that was stimulated to produce hydrogen. In total, we had 174 data points (Fig. 2).

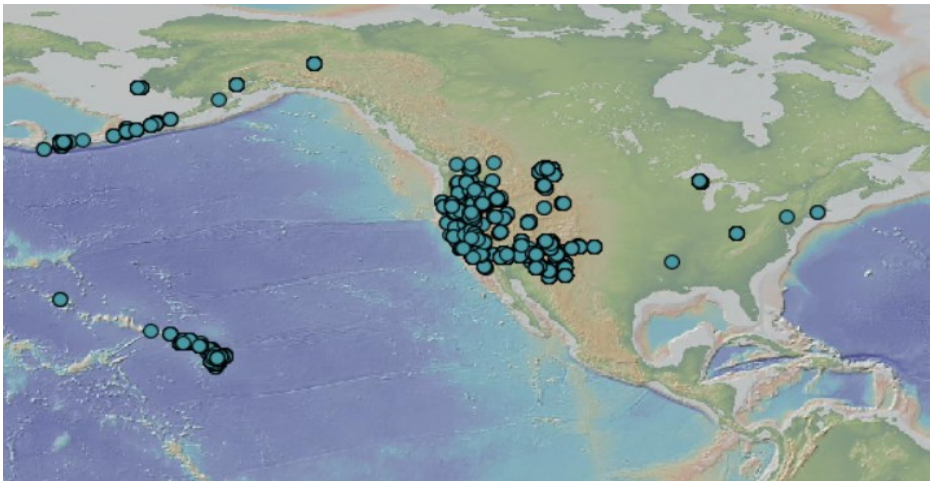

Figure 1: Map showing the bulk download data sample locations from PetDB filtered by country and sample type.

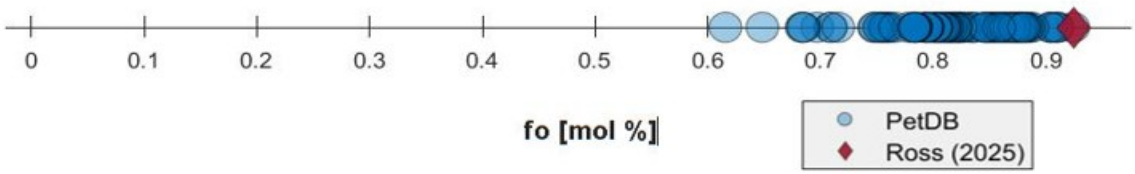

Figure 2: Binary chart of data used in this study distributed according to forsterite (fo, Mg-rich olivine endmember) mole percentage.

Open-source databases such as PetDB could have issues such as misassigning data during entry to the website (Ernst et al., 2025). To validate our data, we compared the minimum and maximum values of each rock type obtained during data acquisition (Table 2) against minimum and maximum values that we compiled from Deer et al. (1997) (Table 1). We highlighted out-of-range values in yellow (Table 2). Also, the correlations: NiO vs. fo (mol %) and NiO vs. Al_2O_3 vs. CaO in data acquisition (Fig. 3) matches charts in Deer et al. (1997) and Chaumba and Roden (2017), where NiO is positively correlated with forsterite content.

Table 1: Minimum and maximum weight percentages of different major oxides in olivine used to benchmark values from PetDB. Values were estimated from Deer et al. (1997).

		SiO_2	**MgO**	**FeO**	**MnO**	**NiO**	**Al_2O_3**	**CaO**	**TiO_2**	**Cr_2O_3**
Ultramafic	Min	39	43	3.0	0.0	0.0	0.0	0.0	0.0	0.0
	Max	42	54	17	0.2	0.7	0.9	0.4	0.1	0.2
Plutonic mafic	Min	29	1.0	13	0.2	-	0.0	0.0	0.0	-
	Max	40	45	67	2.3	-	3.0	1.2	0.8	-
Volcanic mafic	Min	37	38	6.6	0.0	-	-	-	-	-
	Max	41	53	22	0.4	0.6	2.9	0.9	0.4	0.3
Metamorphic	Min	30	0.9	1.0	-	-	-	-	-	-
	Max	42	58	69	0.7	0.5	2.2	2.0	0.5	0.1

Table 2: Minimum and Maximum major oxide data extracted from PetDB in data acquisition step

		SiO_2	MgO	FeO	MnO	TiO_2	Al_2O_3	CaO
Ultramafic	Min	37	30	7.2	0.1	0.0	0.0	0.0
	Max	41	51	33	10	0.1	0.1	0.3
Plutonic mafic	Min	36	32	31	-	-	-	0.1
	Max	36	32	31	-	-	-	0.1
Volcanic mafic	Min	37	33	11	0.1	0.0	0.0	0.2
	Max	41	48	25	0.7	0.1	0.1	0.3
Metamorphic	Min	38	35	22	0.3	0.0	-	0.1
	Max	39	40	27	0.3	0.1	-	0.3

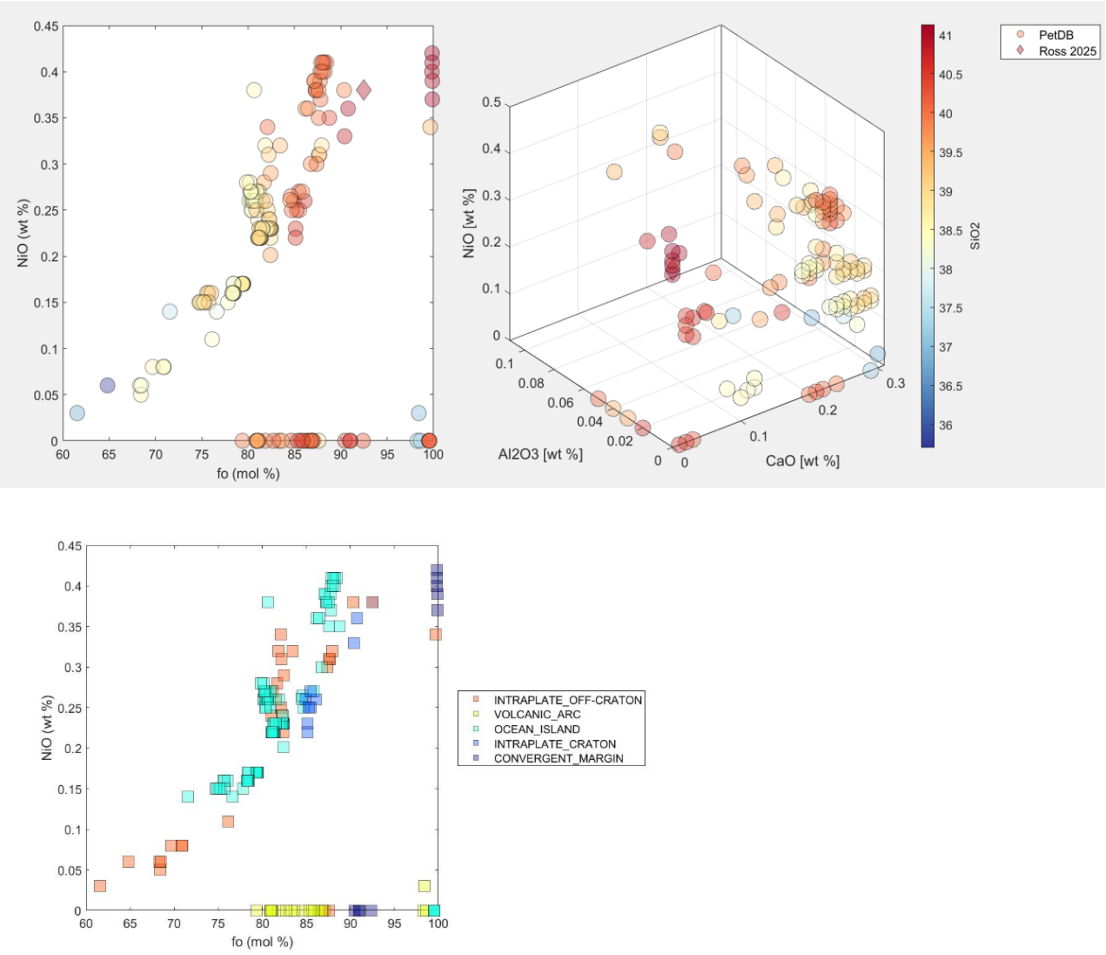

Figure 3: Correlations among different oxides to validate ranges.

3. MINERAL FORMULA RECALCULATION

We conducted mineral formula recalculation in order to convert the major oxide data obtained in data acquisition step into olivine endmember estimates that can be used in geochemical simulation (Discussed in Section 5). The elemental formula for olivine is M_2TO_4, where octahedral site substitution, M = Ca, Mg, Mn^{2+}, Fe^{2+}, Ni, Cr, Fe^{3+}, Ti, and Al and tetrahedral site substitution, T = Fe^{3+}, Al, and Si. The elemental formula was recalculated by assuming no Fe^{3+} because we did not have F_2O_3 measurements. Unlike pyroxene, Fe^{3+} substitution is very common in olivine. Also, normalization in elemental formula recalculation assumed 4 oxygen and 3 cations

Schumacher (1991). Four endmembers were calculated, which are Mg-rich forsterite (Xfo), Fe-rich fayalite (Xfa), Mn-rich tephroite (Xte), and calcium-rich calcio-olivine (XCa-ol). Formula recalculation and endmembers estimation was done in MinplotX (Walters & Gies, 2025).

Our analysis shows less than 0.1 concentration of tephroite and calcio-olivine in all of the olivine samples (ternary diagram in figure 3). Also, NiO (wt %) vs. forsterite (mol %) in figure 4 shows that our samples originated from magmas with different partitioning patterns as evidenced by Ni substitution.

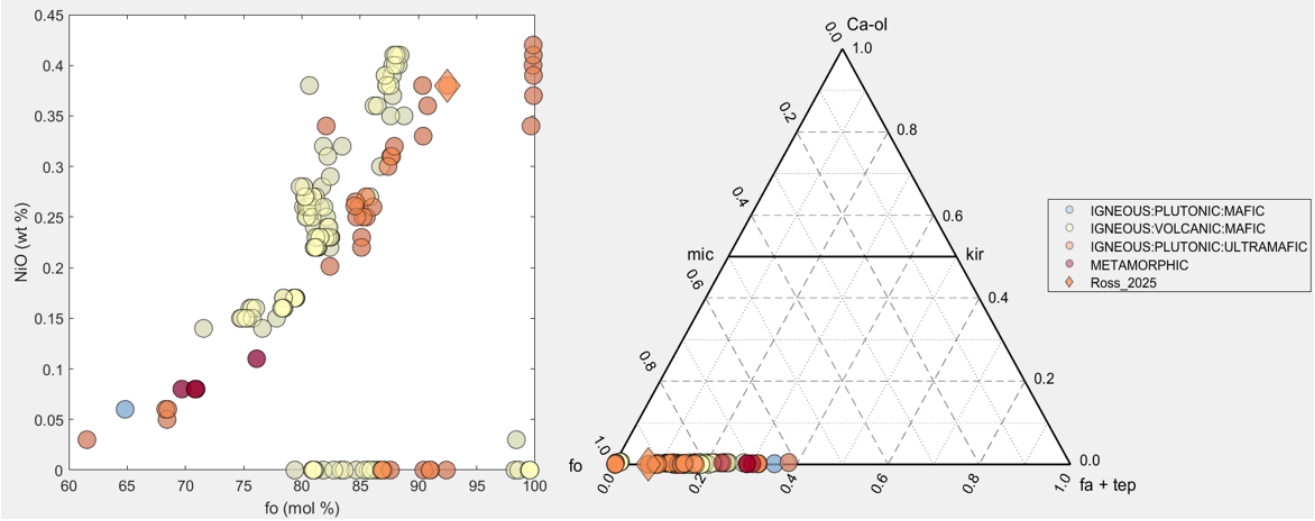

Figure 4: (left) Binary compositional plot showing correlation between NiO (wt %) and forsterite (mol %). (Right) Ternary compositional plot showing four endmembers of olivine.

4. HYDROGEN PRODUCTION MECHANISM

In addition to endmembers estimation in Section 3, a chemical reaction equation is required for geochemical modelling (Section 5). The main mechanism for hydrogen production from Fe- and Mg-rich olivine is through serpentinization (Eq. 1) (Neubeck et al., 2011; Klein and Garrido, 2011; Malvoisin et al., 2012; Grozeva et al., 2017; McCollom et al., 2020):

$$(\mathrm{Fe,\ Mg})_2SiO_4 + v\,H_2O \rightarrow\ w\,(Fe^{II}, Fe^{III}, \mathrm{Mg})_3\,(Si,\ Fe^{III})_2O_5(OH)_4 + y\,Fe^{II}Fe_2^{III}\mathrm{O}_4 + \mathrm{x}\,(\mathrm{Mg}, Fe^{II})(OH)_2 + \mathrm{z}\,\mathrm{H}_2 \quad (1)$$

$$Olivine + Water \rightarrow Serpentine + Magnetite + Brucite + Hydrogen$$

In the limiting case where the fayalite endmember is negligible, the reaction results in olivine dissolution followed by hydration and serpentine formation, without any hydrogen.

In the serpentinization reaction, hydrogen production is most optimal between 200 and 350 °C. At low temperatures (below 150 °C), Carlin et al. (2024) measured hydrogen production from ultramafic rocks through oxidation of ferroan brucite phase. Also, at high temperatures and pressures (500-20000 bars and 1000-1250 °C), Zelenski et al.'s (2022) experimental study showed metasomatism of olivine to produce hydrogen. These details along with hydrogen production from other iron-rich mineral phases, such as ferrous-rich pyroxenes and spinel could be added. Also, brine composition including dissolved gases (N_2, CO_2, SO_2) and salinity would reduce the concentration of dissolved hydrogen.

5. METHODOLOGY

Our objective is to evaluate hydrogen production at different depths where ultramafic, mafic, and metamorphic rocks occur, as is typical in the middle of the earth's crust. We estimated hydrostatic pressure and temperature at three different depths in the mid-crust (5, 10 and 20 km) using density gradients between 100 to 300 bar/km and temperature gradients between 15 to 30 °C/ km. For 20 km estimates, we limited maximum pressure and temperature to 3000 bar and 400 °C, respectively, instead of 6000 bar and 600 °C to avoid the supercritical region as shown in Fig. 5.More rigorous pressure and temperature estimations will be implemented in the future, such as density from mud log and seismic (http://www.usarray.org/) and temperature gradients from the Stanford Thermal Earth Model (Aljubran & Horne, 2024). To obtain hydrogen production in mol/kg of water, we generated 174 2D T-P maps through geochemical batch simulation using rock compositions generated in mineral formula recalculation in MinplotX and parameters in Table 3. Figure 5 shows a summary of our workflow.

Table 3: Input parameters to Reaktoro geochemical batch simulation.

Temperature (°C)	[20, 400]
Pressure (bar)	[100, 3000]
Water to Rock ratio	1
Brine Composition	100% H_2O
Solid Composition	forsterite and fayalite

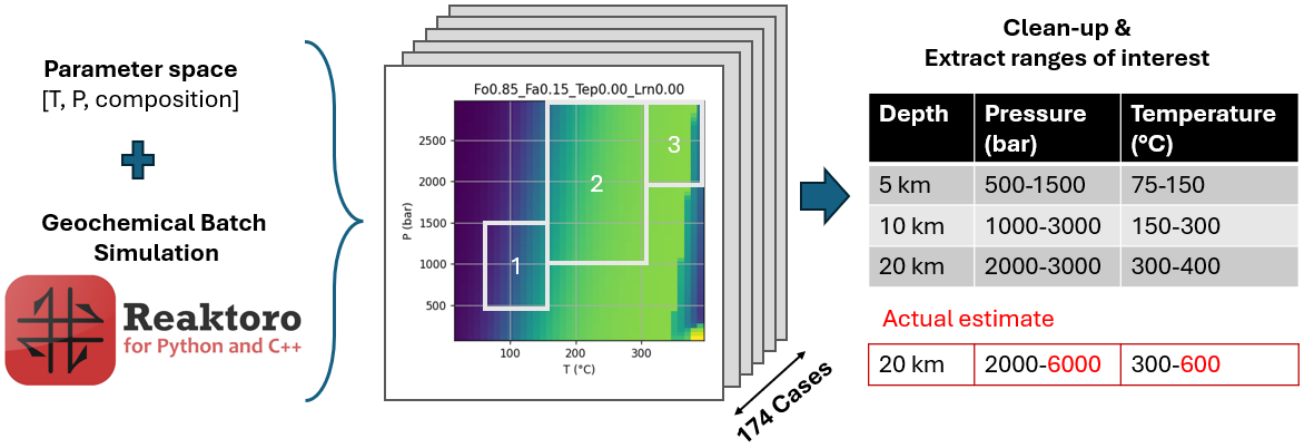

Figure 5: Workflow to obtain depth and hydrogen concentration correlation.

We used Reaktoro (version 2) that is an open-source computational framework (Leal, 2015) for geochemical modelling based on an initial comparison with USGS open source PHREEQC software (version 3). Figure 6 shows that PHREEQC predictions for Fo90 at 500 bars slightly overestimate hydrogen production at temperatures below 200 °C. This could be related to different approaches of modelling the Fo90 olivine solid-solution phase. Specifically, olivine composition was allowed to change in Reaktoro whereas composition was held constant in PHREEQC to force convergence. This assumption is valid for an exchange reaction, which is the case for serpentinization. Also, we note that in both software, the products in Eq. 1 were modelled as binary solid solutions (Mg- and Fe-components) with variable composition as follows: serpentine is chrysotile and greenalite, brucite is brucite since SupcrtBL did not have iron hydroxide, magnetite is magnetite and hematite. Also, the drop-off at 350°C in PHREEQC could be related to differences in thermodynamic data and the water phase-behavior model. Specifically, the LLNL aqueous model and Thermoddem database in PHREEQC uses Helgeson (1969) data which are valid up to 350°C. In contrast, the SUPCRTBL database in Reaktoro is valid up to 1000°C, allowing the simulation to continue more realistically at higher temperatures.

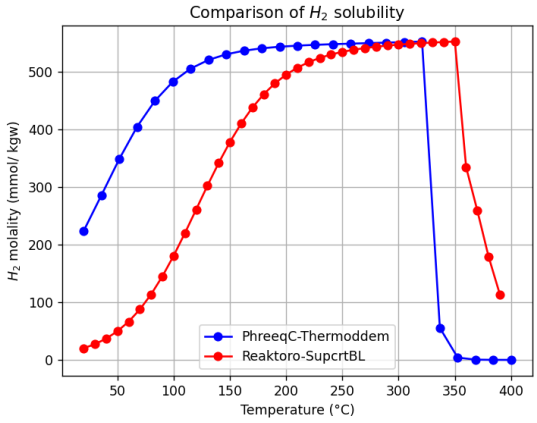

Figure 6: Comparison between batch simulations in Phreeqc (Thermoddem database) and Reaktoro (SupcrtBL database) at 500 bar.

6. RESULTS

Figure 7 (left) shows the sampled hydrogen solubility points at the three depths (5, 10 and 20 km) that were estimated using the workflow in Fig. 5. These points are colored by forsterite content where small forsterite content (light colors) results in greater hydrogen production. We replotted the data (Fig. 7, right) using a violin chart because it is better for interpreting data density when you have overlapping points as in our case. In the violin plot, a wider area corresponds to larger data density. At 5 km, median hydrogen production is around 300 mmol/kg or 600 ppm. At 10 km and 20 km, the brine enters near critical conditions, where hydrogen production and solubility are optimal. As a result, the median jumps to 750 milli-molal (1500 ppm) and 850 milli-molal (1700 ppm). Also, at 20 km, because the sampling area overlaps with the upper limit of serpentinization reaction, where we have a shock. We note that optimal hydrogen production is around a depth of 10 km and forsterite concentration below 0.9. Similarly, optimal conditions for in-house lab data point are within a depth of 10 km. Future work will include associated heat generated during the serpentinization reaction for electricity estimation.

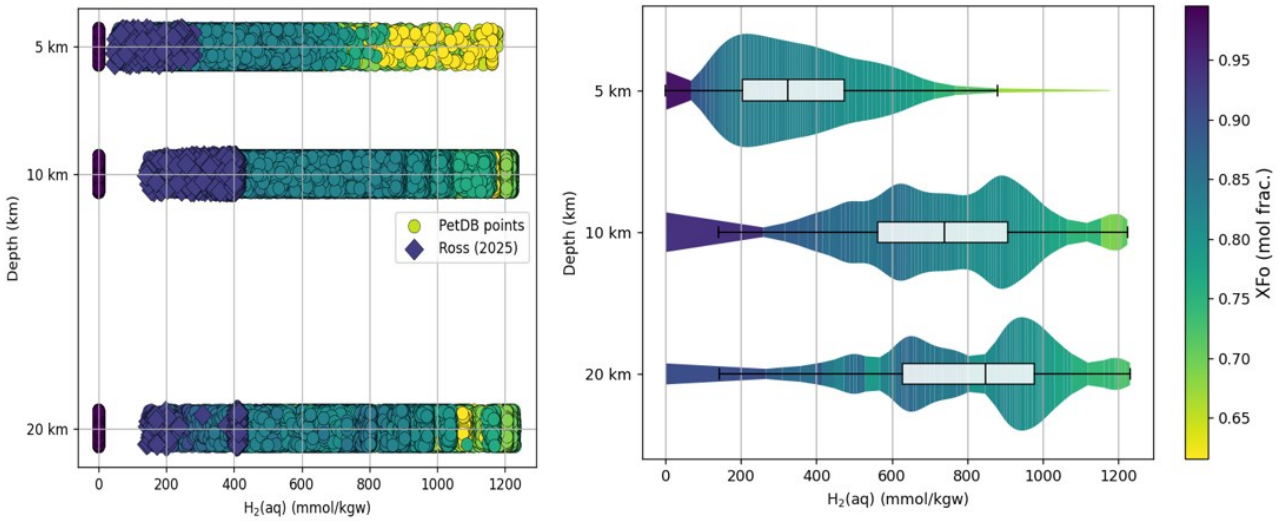

Figure 7: Hydrogen production in mmol per kg water at 5, 10 and 20 km depth. Optimal production occurs at 10 km depth and for forsterite compositions less than 0.9. Right: scatter points. Left: violin chart.

7. CONCLUSION

We demonstrated a workflow for estimating hydrogen production potential from ultramafic, mafic and metamorphic rocks at depths corresponding to the mid-crust. The workflow consists of acquisition of major oxide data from PetDB and in-house experimental results followed by mineral formula and endmember recalculation in MinplotX. Finally, geochemical batch simulation of serpentinization reaction for all data at different ranges of earth hydrostatic pressure and geothermal temperature. Our analysis indicates that the most optimal hydrogen production is at 10 km depth where the temperature is 150-300 °C and forsterite composition below 0.9. Future work will include additional databases, more rigorous geochemical simulations, and estimation of hydrostatic pressure, temperature and depth correlation and heat generated during the serpentinization reaction for electricity estimation.

ACKNOWLEDGEMENT

MMA acknowledges Saudi Aramco for a graduate fellowship and Mohammad J. Aljubran for discussions on hydrogen and geothermal co-production. MMA and ARK thank the SUETRI-A Industrial Affiliates for financial support.

REFERENCES

Aljubran, M. J., and R. N. Horne, *Thermal Earth Model for the Conterminous United States Using an Interpolative Physics-Informed Graph Neural Network*, Geothermal Energy, Springer Nature, Heidelberg, Germany (2024).

Alsinan, M. M., D. Kachuma and A. R. Kovscek, *Thermodynamic Modelling of Hydrogen in Hydrothermal Fluids,* Proceedings, 50th Workshop on Geothermal Reservoir Engineering, Stanford University, Stanford, CA (2025).

Bazarkina, E. F., Chou, I. M., Goncharov, A. F., & Akinfiev, N. N. *The behavior of H2 in aqueous fluids under high temperature and pressure*. Elements, 16(1), 33-38. https://doi.org/10.2138/gselements.16.1.33 (2020).

Buck, C., *The Role of Ammonia at the Coso Geothermal Field*, Proceedings, 50th Workshop on Geothermal Reservoir Engineering, Stanford University, Stanford, CA (2025).

Carlin, W., Malvoisin, B., Brunet, F., Lanson, B., Findling, N., Lanson, M., Fargetton, T., Jeannin, L., and Lhote, O., *Kinetics of Low-Temperature H_2 Production in Ultramafic Rocks by Ferroan Brucite Oxidation*, Geochemical Perspectives Letters, European Association of Geochemistry, Paris, France (2024).

Chaumba J. B. & Roden M. F.(2017), *The Russell Lake Allochthon, East Central Georgia, Southern Appalachians: Mineral Composition Evidence For Its Formation At An Island Arc Setting,* Southeastern Geology 52(3):135-156 (2017).

Deer, W. A., Howie, R. A., & Zussman, J., Rock-Forming Minerals: Volume 1A, Orthosilicates (2nd ed.). Geological Society of London (1997).

Ernst, D. M., Lehnert, K. A., Wörner, G., Traun, M. K., Mues, M., *Screening Method for Rare Earth Element Data - Automated Geochemical Data Assessment,* Goldschmidt (2025)Grozeva, N. G., Klein, F., Seewald, J. S., and Sylva, S. P., *Experimental Study of Carbonate Formation in Oceanic Peridotite*, Geochimica et Cosmochimica Acta, Elsevier, Amsterdam, Netherlands (2017).

Helgeson, H. C., *Thermodynamics of Hydrothermal Systems at Elevated Temperatures and Pressures*, American Journal of Science, Yale University, New Haven, CT (1969).

Klein, F., and Garrido, C. J., *Thermodynamic Constraints on Mineral Carbonation of Serpentinized Peridotite*, Lithos, Elsevier, Amsterdam, Netherlands (2011).

Leal, A. M. M., *Reaktoro: An Open-Source Unified Framework for Modeling Chemically Reactive Systems*, Technical Software Documentation, ETH Zurich, Zurich, Switzerland (2015).

Malvoisin, B., Carlut, J., and Brunet, F., *Serpentinization of Oceanic Peridotites: A High-Sensitivity Method to Monitor Magnetite Production in Hydrothermal Experiments*, Journal of Geophysical Research: Solid Earth, American Geophysical Union, Washington, DC (2012).

McCollom, T. M., Klein, F., Moskowitz, B., Berquó, T. S., Bach, W., and Templeton, A. S., *Hydrogen Generation and Iron Partitioning during Experimental Serpentinization of an Olivine–Pyroxene Mixture*, Geochimica et Cosmochimica Acta, Elsevier, Amsterdam, Netherlands (2020).

Neubeck, A., Duc, N. T., Bastviken, D., Crill, P., and Holm, N. G., *Formation of H_2 and CH_4 by Weathering of Olivine at Temperatures between 30 and 70 °C*, Geochemical Transactions, Springer Nature, Heidelberg, Germany (2011).

Parkhurst, D. L., *User's Guide to PHREEQC: A Computer Program for Speciation, Reaction-Path, Advective-Transport, and Inverse Geochemical Calculations*, U.S. Geological Survey Open-File Report, Denver, CO (2025).

Powell, T., *A Review of Exploration Gas Geothermometry*, Proceedings, 25th Workshop on Geothermal Reservoir Engineering, Stanford University, Stanford, CA (2000).

Ross, C. M., Vega, B., Frouté, L., Kim, T.-W., and Kovscek, A. R., *Hydrogen Generation and Serpentinization of Olivine under Flow Conditions*, Geophysical Research Letters, American Geophysical Union, Washington, DC (2025).

Schumacher, J. C., *Empirical Ferric Iron Corrections: Necessity, Assumptions, and Effects on Selected Geothermobarometers*, Mineralogical Magazine, Mineralogical Society of Great Britain and Ireland, London, UK (1991).

Walters, J. B., *MinPlot: A Mineral Formula Recalculation and Plotting Program for Electron Probe Microanalysis*, Mineralogia, Polish Mineralogical Society, Kraków, Poland (2022).

Walters, J. B., and Gies, N. B., *MinPlotX: A Tool for Formula Recalculation, Visualization, and Comparison of Large Mineral Compositional Datasets*, Mineralogia, Polish Mineralogical Society, Kraków, Poland (2025).

Yardley, B. W. D., and Bodnar, R. J., *Fluids in the Continental Crust*, Geochemical Perspectives, European Association of Geochemistry, Paris, France (2014).

Zelenski, M., Plyasunov, A. V., Kamenetsky, V. S., Nekrylov, N., Matveev, D., and Korneeva, A., *High-Temperature Water–Olivine Interaction and Hydrogen Liberation in the Subarc Mantle*, Contributions to Mineralogy and Petrology, Springer Nature, Heidelberg, Germany (2022).

REFERENCES (PetDB Data Sources)

Bai, Y., Su, B.-X., Xiao, Y., Cui, M.-M., and Charlier, B., *Magnesium and iron isotopic evidence of inter-mineral diffusion in ultramafic cumulates of the Peridotite Zone*, Stillwater Complex, Geochimica et Cosmochimica Acta (2021).

Bergman, S.C., Foland, K.A., and Spera, F.J., *On the origin of an amphibole-rich vein in a peridotite inclusion from the Lunar Crater volcanic field*, Nevada, U.S.A., Earth and Planetary Science Letters (1981).

Brandon, A.D., and Draper, D.S., *Constraints on the origin of the oxidation state of mantle overlying subduction zones: An example from Simcoe*, Washington, USA, Geochimica et Cosmochimica Acta (1996).

Brandon, A.D., Creaser, R.A., Shirey, S.B., and Carlson, R.W., *Osmium recycling in subduction zones*, Science (1996).

Brandon, A.D., Becker, H., Carlson, R.W., and Shirey, S.B., *Isotopic constraints on time scales and mechanisms of slab material transport in the mantle wedge: Evidence from the Simcoe mantle xenoliths*, Washington, USA, Chemical Geology (1999).

Dodson, A., and Brandon, A.D., *Radiogenic helium in xenoliths from Simcoe, Washington, USA: Implications for metasomatic processes in the mantle wedge above subduction zones*, Chemical Geology (1999).

Dodge, F.C.W., Lockwood, J.P., and Calk, L.C., *Fragments of the mantle and crust from beneath the Sierra Nevada batholith: Xenoliths in a volcanic pipe near Big Creek*, California, Geological Society of America Bulletin (1988).

Ducea, M.N., Saleeby, J., Morrison, J., and Valencia, V.A., *Subducted carbonates, metasomatism of mantle wedges and possible connections to diamond formation: An example from California*, American Mineralogist (2005).

Dujardin, A., Demouchy, S., Alard, O., Gardés, E., Laubier, M., and Barou, F., *Ultra-mafic cumulates from Kaupulehu, Hualālai Volcano, Hawai'i: Geochemical resetting of mantle-inherited olivine*, Geochemistry, Geophysics, Geosystems (2025).

Dygert, N., Bernard, R., and Behr, W., *Great Basin mantle xenoliths record active lithospheric downwelling beneath central Nevada*, Geochemistry, Geophysics, Geosystems (2019).

Ehrenberg, S.N., *Rare earth element geochemistry of garnet lherzolite and megacrystalline nodules from minette of the Colorado Plateau province*, Earth and Planetary Science Letters (1982).

Frey, F.A., and Prinz, M., *Ultramafic inclusions from San Carlos, Arizona: Petrologic and geochemical data bearing on their petrogenesis*, Earth and Planetary Science Letters (1978).

Garrison, J.R., and Taylor, L.A., *Megacrysts and xenoliths in kimberlite, Elliott County, Kentucky: A mantle sample from beneath the Permian Appalachian Plateau*, Contributions to Mineralogy and Petrology (1980).

Gaetani, G.A., O'Leary, J., Shimizu, N., Bucholz, C., and Newville, M., *Rapid reequilibration of H_2O and oxygen fugacity in olivine-hosted melt inclusions*, Geology (2012).

Hearn, B.C., Jr., *The Homestead kimberlite: Central Montana, USA: Mineralogy, xenocrysts, and upper-mantle xenoliths*, Lithos (2004).

Lynn, K., and Swanson, D., *Olivine and glass chemistry record cycles of plumbing system recovery after summit collapse events at Kīlauea Volcano, Hawai'i*, Journal of Volcanology and Geothermal Research (2022).

McGuire, A.V., *Southern Basin and Range province crust–mantle boundary: Evidence from gabbroic xenoliths*, Wikieup, Arizona, Journal of Geophysical Research (1994).

Moore, N., Grunder, A., Bohrson, W.A., Carlson, R.W., and Bindeman, I., *Changing mantle sources and the effects of crustal passage on the Steens Basalt*, SE Oregon: Chemical and isotopic constraints, Geochemistry, Geophysics, Geosystems (2020).

Stelling, P., Beget, J., Nye, C.L., Gardner, J.V., Devine, J.D., and George, R., *Geology and petrology of ejecta from the 1999 eruption of Shishaldin Volcano*, Alaska, Bulletin of Volcanology (2002).

Walowski, K., Wallace, P., DeBari, S., Wada, I., Shaw, S., and Rea, J., *Disentangling the roles of subducted volatile contributions and mantle source heterogeneity in the production of magmas beneath the Washington Cascades*, Geochemistry, Geophysics, Geosystems (2024).

Wilshire, H.G., McGuire, A.V., Noller, J.S., and Turrin, B.D., *Petrology of lower crustal and upper mantle xenoliths from the Cima volcanic field, California*, Journal of Petrology (1991).